J. Wind Eng. Ind. Aerodyn. 99 (2011) 154–168

Contents lists available at ScienceDirect

Journal of Wind Engineering and Industrial Aerodynamics

journal homepage: www.elsevier.com/locate/jweia

Large-eddy simulation of atmospheric boundary layer flow through wind turbines and wind farms

Fernando Porté-Agel [a,b,*], Yu-Ting Wu [a,b], Hao Lu [b], Robert J. Conzemius [c]

[a] School of Architecture, Civil and Environmental Engineering (ENAC), École Polytechnique Fédérale de Lausanne (EPFL), 1015 Lausanne, Switzerland
[b] Saint Anthony Falls Laboratory, Department of Civil Engineering, University of Minnesota - Twin Cities, Minneapolis, MN 55414, USA
[c] WindLogics, Inc., 201 4th St. NW, Grand Rapids, MN 55744, USA

ARTICLE INFO

Available online 18 February 2011

Keywords:
Actuator-disk model
Actuator-line model
Blade-element theory
Large-eddy simulation
Wind farm
Wind-turbine wakes

ABSTRACT

Accurate prediction of atmospheric boundary layer (ABL) flow and its interactions with wind turbines and wind farms is critical for optimizing the design (turbine siting) of wind energy projects. Large-eddy simulation (LES) can potentially provide the kind of high-resolution spatial and temporal information needed to maximize wind energy production and minimize fatigue loads in wind farms. However, the accuracy of LESs of ABL flow with wind turbines hinges on our ability to parameterize subgrid-scale (SGS) turbulent fluxes as well as turbine-induced forces. This paper focuses on recent research efforts to develop and validate an LES framework for wind energy applications. SGS fluxes are parameterized using tuning-free Lagrangian scale-dependent dynamic models. These models optimize the local value of the model coefficients based on the dynamics of the resolved scales. The turbine-induced forces (e.g., thrust, lift and drag) are parameterized using two types of models: actuator-disk models that distribute the force loading over the rotor disk, and actuator-line models that distribute the forces along lines that follow the position of the blades. Simulation results are compared to wind-tunnel measurements collected with hot-wire anemometry in the wake of a miniature three-blade wind turbine placed in a boundary layer flow. In general, the characteristics of the turbine wakes simulated with the proposed LES framework are in good agreement with the measurements in the far-wake region. Near the turbine, up to about five rotor diameters downwind, the best performance is obtained with turbine models that induce wake-flow rotation and account for the non-uniformity of the turbine-induced forces. Finally, the LES framework is used to simulate atmospheric boundary-layer flow through an operational wind farm.

1. Introduction

With the fast growing number of wind farms being installed worldwide, the interaction between atmospheric boundary layer (ABL) turbulent flow and wind turbines, and the interference (wake) effects among wind turbines, have become important issues in both the wind energy and the atmospheric science communities (e.g., Petersen et al., 1998; Vermeer et al., 2003; Baidya Roy et al., 2004). Accurate prediction of ABL flow and its interactions with wind turbines is important for optimizing the design (turbine siting) of wind energy projects. In particular, it can be used to maximize wind energy production and minimize fatigue loads in wind farms. Additionally, numerical simulations can provide valuable quantitative insight into the potential impacts of wind farms on local meteorology. These are associated with the significant role of wind turbines in slowing down the wind and enhancing vertical mixing of momentum, heat, moisture and other scalars.

The turbulence parameterization constitutes the most critical part of turbulent flow simulations. It was realized early that direct numerical simulations (DNSs) are not possible for most engineering and environmental turbulent flows, such as the ABL. Thus, the Reynolds-averaged Navier–Stokes (RANS) approach was adopted in most previous studies of ABL flow through stand-alone wind turbines and wind farms (e.g., Xu and Sankar, 2000; Alinot and Masson, 2002; Sørensen et al., 2002; Gómez-Elvira et al., 2005; Tongchitpakdee et al., 2005; Sezer-Uzol and Long, 2006; Kasmi and Masson, 2008). However, as repeatedly reported in a variety of contexts (e.g., AGARD, 1998; Pope, 2000; Sagaut, 2006), RANS computes only the mean flow and parameterizes the effect of all the scales of turbulence. Consequently, RANS is too dependent on the characteristics of particular flows to be used as a method of

* Corresponding author at: School of Architecture, Civil and Environmental Engineering (ENAC), École Polytechnique Fédérale de Lausanne (EPFL), 1015 Lausanne, Switzerland. Tel.: +41 21 6932726; fax: +41 21 6936135.
E-mail address: fernando.porte-agel@epfl.ch (F. Porté-Agel).
URL: http://wire.epfl.ch (F. Porté-Agel).

0167-6105/$ - see front matter © 2011 Elsevier Ltd. All rights reserved.
doi:10.1016/j.jweia.2011.01.011

general applicability. Large-eddy simulation (LES) was developed as an intermediate approach between DNS and RANS, the general idea being that the large, non-universal scales of the flow are computed explicitly, while the small scales are modeled. Large-eddy simulation can potentially provide the kind of high-resolution spatial and temporal information needed to maximize wind energy production and minimize fatigue loads in wind farms. The accuracy of LES in simulations of ABL flow with wind turbines hinges on our ability to parameterize subgrid-scale (SGS) turbulent fluxes as well as turbine-induced forces. Only recently have there been some efforts to apply LES to simulate wind-turbine wakes (Jimenez et al., 2007, 2008; Calaf et al., 2010; Wu and Porté-Agel, 2011).

In this study, we introduce (Section 2) a new LES framework for wind energy applications. The SGS turbulent fluxes of momentum and heat are modeled using the Lagrangian scale-dependent dynamic models, which optimize the local values of the SGS model coefficients and account for their scale dependence in a dynamic manner (using information of the resolved field and, thus, not requiring any tuning of parameters). They have been shown to represent the resolved flow statistics (e.g., mean velocity and energy spectra) near the surface better than the traditional Smagorinsky model or the standard dynamic models (Stoll and Porté-Agel, 2006a, 2008). The turbine-induced forces (e.g., thrust, lift and drag) are parameterized using three wind-turbine models: a standard actuator-disk model without rotation (ADM-NR) that computes an overall thrust force and distributes it uniformly over the rotor disk area; an actuator-disk model with rotation (ADM-R) that computes the local lift and drag forces (based on blade-element momentum theory) and distributes them over the entire rotor disk area; and an actuator-line model (ALM) that calculates those forces along lines that follow the position of the blades. In order to test the performance of the new LES framework (with scale-dependent dynamic models and different turbine parameterizations), simulation results are compared with high-resolution wind-tunnel measurements collected in the wake of a miniature wind turbine in a boundary-layer flow (Section 3). Section 4 presents the application of the new LES framework to a case study of an operational wind farm in Minnesota (USA).

2. LES framework

2.1. Governing equations

LES solves the filtered continuity equation, the filtered Navier–Stokes equations (written here in rotational form and using the Boussinesq approximation), and the filtered heat equation:

$$\frac{\partial \widetilde{u}_i}{\partial x_i} = 0, \tag{1}$$

$$\frac{\partial \widetilde{u}_i}{\partial t} + \widetilde{u}_j\left(\frac{\partial \widetilde{u}_i}{\partial x_j} - \frac{\partial \widetilde{u}_j}{\partial x_i}\right) = -\frac{1}{\rho}\frac{\partial \widetilde{p}^*}{\partial x_i} - \frac{\partial \tau_{ij}}{\partial x_j} + \nu\frac{\partial^2 \widetilde{u}_i}{\partial x_j^2} + \delta_{i3} g\frac{\widetilde{\theta} - \langle \widetilde{\theta} \rangle}{\theta_0} + f_c \varepsilon_{ij3}\widetilde{u}_j - \frac{f_i}{\rho} + \mathcal{F}_i, \tag{2}$$

$$\frac{\partial \widetilde{\theta}}{\partial t} + \widetilde{u}_j\frac{\partial \widetilde{\theta}}{\partial x_j} = -\frac{\partial q_j}{\partial x_j} + \alpha\frac{\partial^2 \widetilde{\theta}}{\partial x_j^2}, \tag{3}$$

where the tilde represents a three-dimensional spatial filtering operation at scale $\widetilde{\Delta}$, $\widetilde{u}_i$ is the resolved velocity in the i-direction (with $i=1, 2, 3$ corresponding to the streamwise (x), spanwise (y) and vertical (z) directions), $\widetilde{\theta}$ is the resolved potential temperature, θ_0 is the reference temperature, the angle brackets represent a horizontal average, g is the gravitational acceleration, f_c is the Coriolis parameter, δ_{ij} is the Kronecker delta, ε_{ijk} is the alternating unit tensor, $\widetilde{p}^* = \widetilde{p} + \frac{1}{2}\rho\widetilde{u}_j\widetilde{u}_j$ is the modified pressure, $\widetilde{p}$ is the filtered pressure, ρ is the air density, ν is the kinematic viscosity of air, α is the thermal diffusivity of air, f_i is an immersed force (per unit volume) for modeling the effect of wind turbines on the flow, and $\mathcal{F}_i$ is a forcing term (e.g., a mean pressure gradient). Based on the Boussinesq approximation, both ρ and θ_0 in Eq. (2) are assumed to be constant. τ_{ij} and q_j are the SGS fluxes of momentum and heat, respectively, and are defined as

$$\tau_{ij} = \widetilde{u_i u_j} - \widetilde{u}_i\widetilde{u}_j \tag{4}$$

and

$$q_j = \widetilde{u_j\theta} - \widetilde{u}_j\widetilde{\theta}. \tag{5}$$

These SGS fluxes are unknown in a simulation and, therefore, they need to be parameterized. Next, we describe their parameterization using Lagrangian scale-dependent dynamic models.

2.2. Lagrangian scale-dependent dynamic models

A common parameterization approach in LES consists of computing the deviatoric part of the SGS stress with an eddy-viscosity model

$$\tau_{ij} - \tfrac{1}{3}\tau_{kk}\delta_{ij} = -2\nu_{sgs}\widetilde{S}_{ij}, \tag{6}$$

and the SGS heat flux with an eddy-diffusivity model

$$q_j = -\frac{\nu_{sgs}}{Pr_{sgs}}\frac{\partial \widetilde{\theta}}{\partial x_j}, \tag{7}$$

where $\widetilde{S}_{ij} = (\partial\widetilde{u}_i/\partial x_j + \partial\widetilde{u}_j/\partial x_i)/2$ is the resolved strain rate tensor, ν_{sgs} is the SGS eddy viscosity and Pr_{sgs} is the SGS Prandtl number. A popular way of modeling the eddy viscosity is to use the mixing length approximation (Smagorinsky, 1963). In particular, the eddy viscosity is modeled as $\nu_{sgs} = C_s^2\widetilde{\Delta}^2|\widetilde{S}|$, where $|\widetilde{S}| = (2\widetilde{S}_{ij}\widetilde{S}_{ij})^{1/2}$ is the strain rate magnitude, and C_s is the Smagorinsky coefficient. When applied to calculate the SGS heat flux, the resulting eddy-diffusivity model requires the specification of the lumped coefficient $C_s^2 Pr_{sgs}^{-1}$.

One of the main challenges in the implementation of the eddy-viscosity/diffusivity models is the specification of the model coefficients. The values of C_s and Pr_{sgs} (and therefore $C_s^2 Pr_{sgs}^{-1}$) are well established for isotropic turbulence. In that case, if a cut-off filter is used in the inertial subrange and the filter scale $\widetilde{\Delta}$ is equal to the grid size, then $C_s \approx 0.17$ and $Pr_{sgs} \approx 0.4$ (Lilly, 1967; Mason and Derbyshire, 1990). However, anisotropy of the flow, particularly the presence of a strong mean shear near the surface in high-Reynolds-number ABLs, makes the optimum value of those coefficients depart from their isotropic counterparts (e.g., Kleissl et al., 2003, 2004; Bou-Zeid et al., 2008). A common practice is to specify the coefficients in an *ad hoc* fashion. For C_s, this typically involves the use of dampening functions and stability corrections based on model performance and field data (e.g., Mason and Thomson, 1992; Mason, 1994; Kleissl et al., 2003, 2004). Similarly, a stability dependence is usually prescribed for the SGS Prandtl number, with values ranging from about 0.3 to 0.4 for convective and near-neutral conditions to about 1 under very stable stratification (e.g., Mason and Brown, 1999).

An alternative was introduced by Germano et al. (1991) in the form of the dynamic Smagorinsky model, in which C_s is calculated based on the resolved flow field using a test filter ($\overline{f}$) at scale $\overline{\Delta} = \alpha\widetilde{\Delta}$ (with typically $\alpha = 2$). This procedure was also applied to the eddy-diffusivity model by Moin et al. (1991) to calculate the lumped coefficient. While the dynamic model removes the need for prescribed stability and shear dependence, it assumes that the

model coefficients are scale invariant. Simulations (e.g., Porté-Agel et al., 2000; Porté-Agel, 2004) and experiments (e.g., Porté-Agel et al., 2001; Bou-Zeid et al., 2008) have shown that the scale invariance assumption breaks down near the surface, where the filter and/or test filter scales fall outside of the inertial subrange of the turbulence.

The assumption of scale invariance in the standard dynamic model was relaxed by Porté-Agel et al. (2000) and Porté-Agel (2004) through the development of scale-dependent dynamic models for the SGS fluxes of momentum and heat, respectively. It is important to note that dynamic procedures require some sort of averaging (over horizontal planes, local or Lagrangian) to guarantee numerical stability. Lagrangian averaging, as introduced by Meneveau et al. (1996), is best suited for LESs of complex ABL flows (where there is no direction of flow homogeneity).

In this study, we employ tuning-free Lagrangian scale-dependent dynamic models (Stoll and Porté-Agel, 2006a, 2008) to compute the optimized local values of the model coefficients C_s and Pr_{sgs}. Based on the Germano identity (Germano et al., 1991; Lilly, 1992), minimization of the error associated with the use of the model equations (6) and (7) results in the following equations:

$$C_s^2(\widetilde{\Delta}) = \frac{\langle L_{ij}M_{ij}\rangle_{\mathcal{L}}}{\langle M_{ij}M_{ij}\rangle_{\mathcal{L}}}, \tag{8}$$

$$C_s^2 Pr_{sgs}^{-1}(\widetilde{\Delta}) = \frac{\langle K_i X_i\rangle_{\mathcal{L}}}{\langle X_i X_i\rangle_{\mathcal{L}}}, \tag{9}$$

where $\langle\cdot\rangle_{\mathcal{L}}$ denotes Lagrangian averaging (Meneveau et al., 1996; Stoll and Porté-Agel, 2006a), $L_{ij} = \widetilde{\overline{u}_i\overline{u}_j} - \widetilde{\overline{u}}_i\widetilde{\overline{u}}_j$, $M_{ij} = 2\widetilde{\Delta}^2(\widetilde{|\overline{S}|\overline{S}_{ij}} - \alpha^2\beta|\widetilde{\overline{S}}|\widetilde{\overline{S}}_{ij})$, $K_i = \widetilde{\overline{u}\overline{\theta}} - \widetilde{\overline{u}}_i\widetilde{\overline{\theta}}$, and $X_i = \widetilde{\Delta}^2(\widetilde{|\overline{S}|\partial\overline{\theta}/\partial x_i} - \alpha^2\beta_\theta|\widetilde{\overline{S}}|\partial\widetilde{\overline{\theta}}/\partial x_i)$. Here, $\beta = C_s^2(\alpha\widetilde{\Delta})/C_s^2(\widetilde{\Delta})$ and $\beta_\theta = C_s^2 Pr_{sgs}^{-1}(\alpha\widetilde{\Delta})/C_s^2 Pr_{sgs}^{-1}(\widetilde{\Delta})$ are the scale-dependence parameters, defined as the ratio between the coefficients at the test filter scale and at the filter scale. Instead of assuming $\beta = 1$ and $\beta_\theta = 1$ as scale-invariant models do, the Lagrangian scale-dependent dynamic models leave the two parameters as unknowns that will be calculated dynamically. Solution for β and β_θ requires to use a second test filter ($\widehat{f}$) at scale $\widehat{\Delta} = \alpha^2\widetilde{\Delta}$. In addition, the procedure assumes a power-law dependence of the coefficients with scale, and thus

$$\beta = \frac{C_s^2(\alpha\widetilde{\Delta})}{C_s^2(\widetilde{\Delta})} = \frac{C_s^2(\alpha^2\widetilde{\Delta})}{C_s^2(\alpha\widetilde{\Delta})}, \tag{10}$$

$$\beta_\theta = \frac{C_s^2 Pr_{sgs}^{-1}(\alpha\widetilde{\Delta})}{C_s^2 Pr_{sgs}^{-1}(\widetilde{\Delta})} = \frac{C_s^2 Pr_{sgs}^{-1}(\alpha^2\widetilde{\Delta})}{C_s^2 Pr_{sgs}^{-1}(\alpha\widetilde{\Delta})}. \tag{11}$$

It is important to note that this assumption is much weaker than the assumption of scale invariance ($\beta = 1$ and $\beta_\theta = 1$) in scale-invariant models, such as the standard dynamic Smagorinsky model, and it has been shown to be more realistic in recent *a-priori* field studies (e.g., Bou-Zeid et al., 2008). Again minimizing the error associated with the use of the model equations (6) and (7), another set of equations for C_s and Pr_{sgs} is obtained:

$$C_s^2(\widetilde{\Delta}) = \frac{\langle L'_{ij}M'_{ij}\rangle_{\mathcal{L}}}{\langle M'_{ij}M'_{ij}\rangle_{\mathcal{L}}}, \tag{12}$$

$$C_s^2 Pr_{sgs}^{-1}(\widetilde{\Delta}) = \frac{\langle K'_i X'_i\rangle_{\mathcal{L}}}{\langle X'_i X'_i\rangle_{\mathcal{L}}}, \tag{13}$$

where $L'_{ij} = \widehat{\widetilde{u}_i\widetilde{u}_j} - \widehat{\widetilde{u}}_i\widehat{\widetilde{u}}_j$, $M'_{ij} = 2\widehat{\widetilde{\Delta}}^2(\widehat{|\widetilde{S}|\widetilde{S}_{ij}} - \alpha^2\beta^2|\widehat{\widetilde{S}}|\widehat{\widetilde{S}}_{ij})$, $K'_i = \widehat{\widetilde{u}\widetilde{\theta}} - \widehat{\widetilde{u}}_i\widehat{\widetilde{\theta}}$, and $X'_i = \widehat{\widetilde{\Delta}}^2(\widehat{|\widetilde{S}|\partial\widetilde{\theta}/\partial x_i} - \alpha^2\beta_\theta^2|\widehat{\widetilde{S}}|\partial\widehat{\widetilde{\theta}}/\partial x_i)$. More details can be found in Porté-Agel et al. (2000), Porté-Agel (2004), Stoll and Porté-Agel (2006a) and Stoll and Porté-Agel (2008).

Tests of different averaging procedures (over horizontal planes, local and Lagrangian) simulations of a stable boundary layer with the scale-dependent dynamic model have shown that the Lagrangian averaging produces the best combination of self-consistent model coefficients, first- and second-order flow statistics, and small sensitivity to grid resolution (Stoll and Porté-Agel, 2008). Based on the local dynamics of the resolved scales, these tuning-free models compute C_s and Pr_{sgs} dynamically as the flow evolves in both space and time. This makes the models well suited for simulations of ABL flow over heterogeneous terrain.

The Lagrangian scale-dependent dynamic models have also been used to compute C_S and $C_S^2\,Pr_{sgs}^{-1}$ in simulations of neutral and stable boundary layers over simple topography patterns (using terrain following coordinates) consisting of two-dimensional sinusoidal hills (Wan et al., 2007) and single hills (Wan and Porté-Agel, 2011). As illustrated in Fig. 1a, the model for the SGS stress tensor is able to dynamically (without tuning) adjust the value of the Smagorinsky coefficient and scale-dependence coefficient β to have smaller values near the hill crest, where the flow is more anisotropic. As a result, it yields results that are more accurate and less dependent on resolution than the standard Smagorinsky and scale-invariant dynamic models (see Fig. 2 for the prediction of the velocity profile above the hill crest). More details on these simulation results can be found in Wan et al. (2007) and Wan and Porté-Agel (2011).

2.3. Boundary conditions

The surface boundary conditions require calculating the instantaneous local surface shear stress and heat flux at each

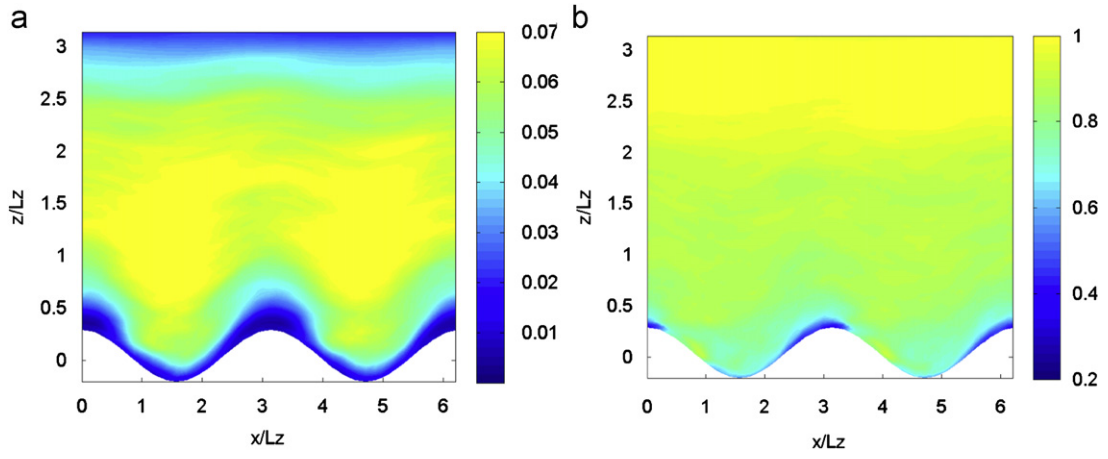

Fig. 1. (a) Smagorinsky coefficient (C_S^2) obtained with the Lagrangian scale-dependent dynamic model for the SGS stress tensor; (b) scale-dependence parameter (β) obtained with the Lagrangian scale-dependent dynamic model for the SGS stress tensor. Results are averaged over time and spanwise direction.

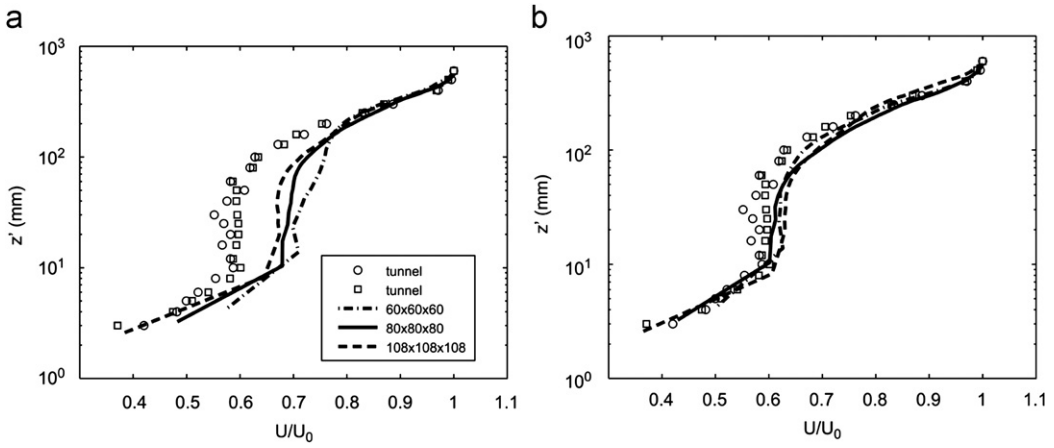

Fig. 2. Effect of grid resolution on the simulated non-dimensional velocity profile over the wave crest obtained from (a) the Lagrangian dynamic model and (b) the Lagrangian scale-dependent dynamic model for the SGS stress tensor. The wind-tunnel data of Gong et al. (1996) (symbols) are also shown.

surface grid point. This is accomplished through the application of Monin–Obukhov similarity theory (Businger et al., 1971) between the surface and the first vertical grid point immediately above. Although this theory is strictly only valid for average quantities under steady and homogeneous conditions, it is commonly applied to fluctuating (filtered) quantities in LES of ABL flows (Moeng, 1984; Albertson and Parlange, 1999; Stoll and Porté-Agel, 2006b, 2008). In particular, the surface shear stress $\tau_{(\beta,s)}(x,y,t)$ (where $i=1, 2$) is computed as follows:

$$\tau_{i3,s}(x,y,t) = -\left[\frac{\kappa\widetilde{u}_r(x,y,z,t)}{\ln(z/z_0)-\Psi_M(z/L)+\Psi_M(z_0/L)}\right]^2 \frac{\widetilde{u}_i(x,y,z,t)}{\widetilde{u}_r(x,y,z,t)}, \tag{14}$$

where the subscript s denotes surface values, $\widetilde{u}_r(x,y,z,t) = [\widetilde{u}_1(x,y,z,t)^2+\widetilde{u}_2(x,y,z,t)^2]^{1/2}$ is the local instantaneous (filtered) horizontal velocity magnitude at height $z=\Delta_z/2$ with Δ_z corresponding to the vertical grid spacing, κ is the von Kármán constant, z_0 is the aerodynamic roughness length, L is the Obukhov length and Ψ_M is the momentum stability correction function.

The instantaneous (filtered) potential temperature at $z=\Delta_z/2$ is used for the local surface heat flux $q_{3,s}(x,y,t)$ parameterization:

$$q_{3,s}(x,y,t) = \frac{\kappa\widetilde{u}_*[\theta_r(x,y,z,t)-\widetilde{\theta}(x,y,z,t)]}{\ln(z/z_r)-\Psi_H(z/L)+\Psi_H(z_0/L)}, \tag{15}$$

where $\widetilde{u}_* = [\tau_{13,s}(x,y,t)^2+\tau_{23,s}(x,y,t)^2]^{1/4}$ is the local surface friction velocity, z_r is a reference height for the surface temperature, $\theta_r(x,y,z,t)$ is the local potential temperature at that height, and Ψ_H is the stability correction function for temperature. In Eqs. (14) and (15), both stability correction functions are calculated at every point based on a locally defined Obukhov length,

$$L = \frac{-\widetilde{u}_*^3\widetilde{\theta}}{\kappa g q_{3,s}}. \tag{16}$$

The correction functions suggested by Arya (2001) are selected here. They are given as $\Psi_M(z/L)=\Psi_H(z/L)=0$ for neutral conditions, $\Psi_M(z/L)=\Psi_H(z/L)=-5(z/L)$ for stable conditions, and $\Psi_M(z/L) = \ln[(1+x^2)(1+x)^2/8]-2\tan^{-1}(x)+\pi/2$ and $\Psi_H(z/L) = -2\ln[(1+x^2)/2]$ for unstable conditions. Here, $x=(1-15z/L)^{1/4}$. The upper boundary condition is a zero flux condition.

2.4. Wind-turbine parameterizations

The actuator-disk model is a straightforward approach to represent the wind-turbine forces in numerical models of flow through propellers and turbines. The approach was introduced by Froude (1889) as a continuation of the work of Rankine (1865) on momentum theory of propellers. The Rankine–Froude actuator-disk model assumes the load is distributed uniformly over the circular rotor disk. Since the resulting force acts only in the axial direction (i.e., no rotational component is considered), here we refer to this method as 'actuator-disk model without rotation' (ADM-NR). The axial thrust force F_x acting on the actuator disk in the streamwise direction is modeled as $F_x = \frac{1}{2}\rho\widetilde{u}_0^2 A C_T$, where $\widetilde{u}_0$ is the unperturbed resolved velocity of the axial incident flow in the center of the rotor disk, A is the frontal area of the cells within the rotor region and C_T is the thrust coefficient. This model provides only a one-dimensional approximation of the turbine-induced thrust force; however, due to its simplicity and capability to deliver reasonable results with coarse grids, this model is still widely used in the context of both RANS (e.g., Gómez-Elvira et al., 2005) and, more recently, also LES (Jimenez et al., 2007, 2008; Calaf et al., 2010; Wu and Porté-Agel, 2011).

A major advancement in wind-turbine modeling was the introduction of the blade-element momentum (BEM) theory (Glauert, 1963). Since the flow is assumed to be inviscid, the blade-element approach does not require resolving the boundary-layer flow around the turbine blade surface, which greatly reduces the computational cost requirements. In Fig. 3c, a cross-section element at radius r defines the airfoil in the (θ,x) plane, where x is the streamwise direction. Denoting the tangential and axial velocities in the inertial frame of reference as V_θ and V_x, respectively, the local velocity relative to the rotating blade is given as $\mathbf{V}_{rel} = (V_\theta-\Omega r, V_x)$. The angle of attack is defined as $\alpha=\varphi-\gamma$, where $\varphi = \tan^{-1}(V_x/(\Omega r-V_\theta))$ is the angle between $\mathbf{V}_{rel}$ and the rotor plane, and γ is the local pitch angle. The actuator-disk surface is defined as the area swept by the blades, where the turbine-induced lift and drag forces are parameterized and integrated over the rotor disk. Here we refer to this method as 'actuator-disk model with rotation' (ADM-R). Unlike the ADM-NR, the ADM-R considers the effect of the turbine-induced flow rotation as well as the non-uniform force distribution. To further determine the forces acting on the rotor disk, we consider an annular area of differential size $dA = 2\pi r\, dr$. The resulting force is given by

$$\mathbf{f}_{2D} = \frac{d\mathbf{F}}{dA} = \frac{1}{2}\rho V_{rel}^2 \frac{Bc}{2\pi r}(C_L\mathbf{e}_L + C_D\mathbf{e}_D), \tag{17}$$

where B is the number of blades, $C_L = C_L(\alpha,Re)$ and $C_D = C_D(\alpha,Re)$ are the lift coefficient and the drag coefficient, respectively, c is the chord length, and $\mathbf{e}_L$ and $\mathbf{e}_D$ denote the unit vectors in the directions of the lift and the drag, respectively. More details on both actuator-disk models are given by Wu and Porté-Agel (2011).

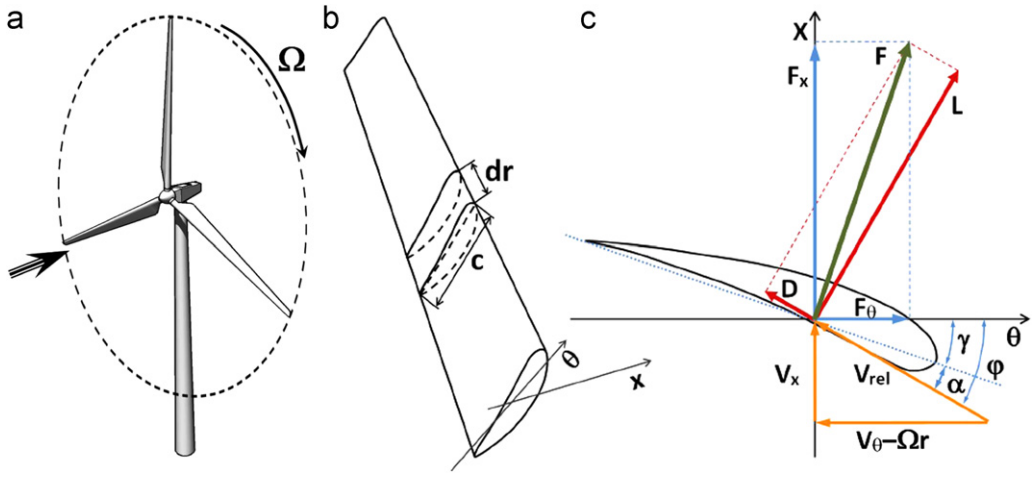

Fig. 3. Schematic of the blade-element momentum approach: (a) three-dimensional view of a wind turbine; (b) a discretized blade; and (c) cross-section airfoil element showing velocities and force vectors.

In the generalized actuator-disk and related models, the turbine-induced forces (lift, drag and thrust) are parameterized and integrated over the entire rotor disk, making it impossible to capture helicoidal tip vortices (Vermeer et al., 2003). To overcome this limitation, a three-dimensional actuator-line model (ALM) was developed by Sørensen and Shen (2002). The ALM uses BEM theory to calculate the turbine-induced lift and drag forces and distributes them along lines representing the blades. As a result, it has the ability to capture important features of turbine wakes, such as tip vortices and coherent periodic helicoidal vortices in the near-wake region (Sørensen and Shen, 2002; Troldborg et al., 2007; Ivanell et al., 2009). The resulting turbine-induced force is calculated as

$$\mathbf{f}_{1D} = \frac{d\mathbf{F}}{dr} = \frac{1}{2}\rho V_{rel}^2 c(C_L\mathbf{e}_L + C_D\mathbf{e}_D). \tag{18}$$

In the above-mentioned wind-turbine models, the blade-induced forces are distributed smoothly to avoid singular behavior and numerical instability. In practice, these forces are distributed in a three-dimensional Gaussian manner by taking the convolution of the computed local load, **f**, and a regularization kernel η_ε as shown below:

$$\mathbf{f}^\varepsilon = \frac{1}{\Delta v}(\mathbf{F}\otimes\eta_\varepsilon), \quad \eta_\varepsilon = \frac{1}{\varepsilon^3\pi^{3/2}}\exp\left(-\frac{r_p{}^2}{\varepsilon^2}\right), \tag{19}$$

where Δv is the volume of a grid cell, r_p is the distance between grid points and points representing the actuator disk or the actuator line, and ε is a parameter that adjusts the distribution of the regularized load.

The main advantage of representing the blades by airfoil data is that much fewer grid points are needed to capture the influence of the blades compared to what would be needed for simulating the actual geometry of the blades. Therefore, the ADM-R and ALM are well suited for studies of turbine wakes (from stand-alone or multiple turbines) that require simulating large domains to capture all the important scales of both ABL and turbine wake flows, while keeping the computing cost at a reasonable level.

The effects of the nacelle and the turbine tower on the turbulent flow are modeled as drag forces $\mathbf{f}^{nacelle}$ and $\mathbf{f}^{tower}$, respectively, by using a formulation similar to the ADM-NR and a drag coefficient based on the specific geometry. More details on this approach are given by Wu and Porté-Agel (2011). As a result, the total immersed force f_i associated with wind-turbine effects in the filtered momentum equation (Eq. (2)) is given by

$$f_i = (\mathbf{f}^\varepsilon + \mathbf{f}^{nacelle} + \mathbf{f}^{tower})\cdot\mathbf{e}_i, \tag{20}$$

where $\mathbf{e}_i$ is the unit vector in the i-th direction.

3. Validation of the LES framework

In this section, the above-described LES framework is validated using high-resolution velocity measurements collected in the wake of a three-blade miniature wind turbine placed in a wind-tunnel boundary layer flow. The experiment is described by Chamorro and Porté-Agel (2010). A modified version of the LES code described by Albertson and Parlange (1999), Porté-Agel et al. (2000), Porté-Agel (2004) and Stoll and Porté-Agel (2006a) is used. In this study, the three wind-turbine models (ADM-NR, ADM-R and ALM) for the turbine-induced forces are implemented in the LES code and used to simulate the wind-tunnel case, i.e., a neutral boundary-layer flow through a stand-alone wind turbine over a flat homogeneous surface. The main features of the code and a brief description of the case study are given below. More details on the numerical setup are provided by Wu and Porté-Agel (2011).

3.1. Numerical setup

As shown in Fig. 4, the computational domain has a height L_z=0.460 m, corresponding to the top of the boundary layer H. The horizontal computational domain spans a distance L_x=4.320 m in the streamwise direction and L_y = 0.720 m in the spanwise direction. The domain is divided uniformly into $N_x \times N_y \times N_z = 192 \times 32 \times 42$ grid points. The grid arrangement is staggered in the vertical direction with the first level of computation for the vertical velocity $\widetilde{w}$ at a height of $\Delta_z = L_z/(N_z-1)$ and the first level for $\widetilde{u}$, $\widetilde{v}$ and $\widetilde{p}^*$ at $\Delta_z/2$. The LES code uses a hybrid pseudospectral finite-difference method, i.e., spatial derivatives are computed using pseudospectral methods in the horizontal directions and finite differences in the vertical direction. Time advancement is discretized using an explicit second-order Adams–Bashforth scheme. Lateral boundary conditions are periodic, which is a seamless choice for pseudospectral methods. The bottom and top boundary conditions are described in Section 2.3. The flow is driven by a constant streamwise pressure gradient. The friction velocity and aerodynamic surface roughness are 0.102 m/s and 0.03 mm, respectively.

The wind turbine used by Chamorro and Porté-Agel (2010) in the wind-tunnel experiment consists of a three-blade GWS/EP-6030 × 3 rotor attached to a small DC generator motor. The rotor diameter d and the hub height H_{hub} of the turbine are 0.150 m and 0.125 m, respectively. In the simulations, the blade section is viewed as a flat plate, whose lift and drag coefficients are determined based on a previous experimental study by Sunada et al. (1997). The radial variation of the chord length and pitch angle of the turbine blade is given by Wu and Porté-Agel (2011). The wind turbine is placed in the middle of the computational domain at a distance of six rotor diameters from the upstream boundary. To avoid that the flow upwind of the turbine is influenced by the turbine-induced wake flow (due to the periodic boundary conditions), we adopt a buffer zone (Fig. 4) to adjust the flow from the very-far-wake downwind condition to that of an undisturbed boundary layer inflow condition. This inflow condition is obtained from a separate simulation of the boundary-layer flow corresponding to the upwind of the wind turbine in the wind-tunnel experiment of Chamorro and Porté-Agel (2010).

3.2. Comparison with wind-tunnel measurements

Each of the simulations performed with the three wind turbine models (ADM-NR, ADM-R and ALM) was run for a total duration of four physical minutes, with converged turbulence statistics averaged over the last two minutes. The spatial distribution of two key turbulence statistics is used to characterize wind-turbine wakes: the time-averaged streamwise velocity $\overline{u}$ and the streamwise turbulence intensity $\sigma_u/\overline{u}_{hub}$. The over-bar represents a temporal average. The experimental data were collected at $x/d = -1, 1, 2, \ldots, 9, 10, 12, \ldots, 18, 20$ in the middle of the domain as well as $y/d = -0.7, -0.6, \ldots, 0.6, 0.7$ in a cross-section downwind of the turbine at $x/d = 5$. Fig. 5 shows contours of the time-averaged streamwise velocity

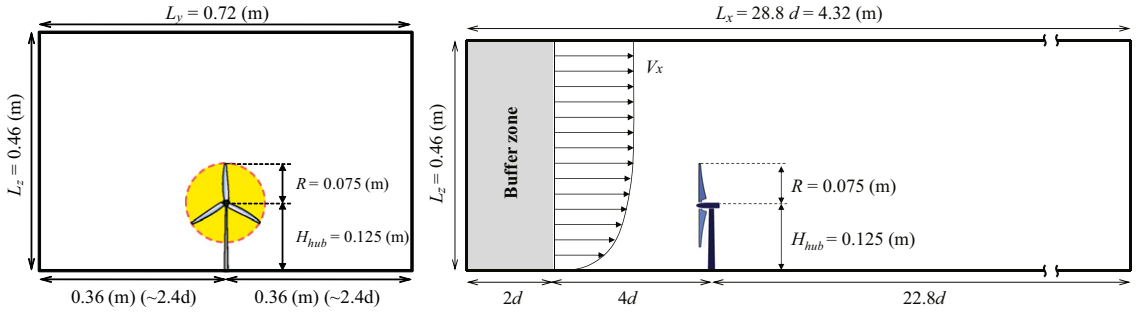

Fig. 4. Schematic of the simulation domain. Front view (left) and side view (right).

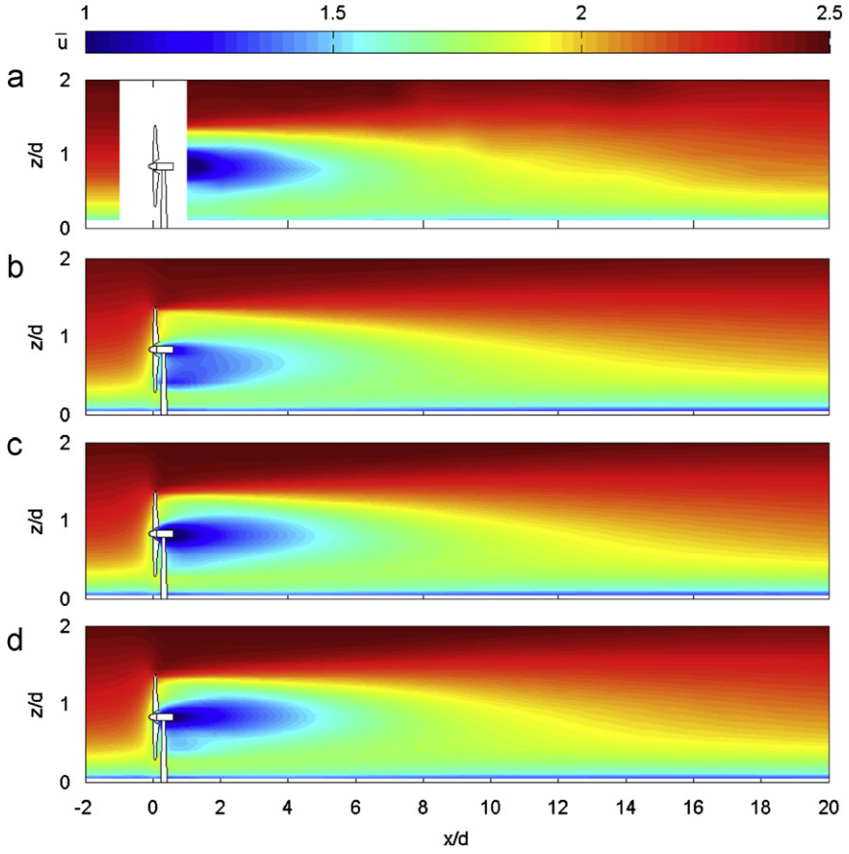

Fig. 5. Contours of the time-averaged streamwise velocity $\overline{u}$ (m/s) in the middle vertical plane perpendicular to the turbine: (a) wind-tunnel measurements, (b) ADM-NR, (c) ADM-R and (d) ALM.

obtained from the wind-tunnel experiment and simulations with the ADM-NR, ADM-R and ALM on a vertical plane perpendicular to the turbine. Furthermore, to facilitate the quantitative comparison of the results, Fig. 6 shows vertical profiles of the measured and simulated time-averaged streamwise velocity at selected downwind locations ($x/d=2, 3, 5, 7, 10, 14, 20$), together with the incoming flow velocity profile. There is a clear evidence of the effect of the turbine extracting momentum from the incoming flow and producing a wake (region of reduced velocity) immediately downwind. As expected, the velocity deficit (reduction with respect to the incoming flow) is largest near the turbine and it becomes smaller as the wake expands and entrains surrounding air. Nonetheless, the effect of the wake is still noticeable even in the far wake, at distances as large as $x/d=20$. Further, due to the non-uniform (logarithmic) mean velocity profile of the incoming boundary-layer flow, we find a non-axisymmetric distribution of the mean velocity profile and, consequently, of the mean shear in the turbine wake. In particular, as also reported by Chamorro and Porté-Agel (2009, 2010), the strongest shear (and the associated turbulence kinetic energy production) is found at the level of the top tip. This result contrasts with the axisymmetry of the turbulence statistics reported by previous studies in the case of wakes of turbines placed in free-stream flows (Crespo and Hernández, 1996; Medici and Alfredsson, 2006; Troldborg et al., 2007), and demonstrates the substantial influence of the incoming flow on the structure and dynamics of wind-turbine wakes.

As shown in Figs. 5 and 6, the LES results obtained from the ADM-R and ALM show that the mean velocity profiles are in good agreement with the measurements everywhere in the turbine wake (near wake as well as far wake). The ADM-NR is able to capture the velocity distribution in the far-wake region ($x/d>5$), but it clearly overpredicts the velocity in the center of the wake in the near-wake region ($x/d<5$). This failure of the ADM-NR to reproduce the velocity magnitude in the near-wake region can be attributed to the limitations of two important assumptions made in the ADM-NR (but not in the other wind-turbine models): (a) the effect of turbine-induced rotation is ignored, and (b) the force is uniformly distributed over the rotor disk, thus ignoring the radial variation of the force. These two assumptions are in contrast with simulation results of the non-uniform force distribution reported by Sørensen and Shen (2002). It is important to note that, as discussed by Wu and Porté-Agel (2011), accounting for the non-uniform distribution of the thrust force is responsible for most of the improvement observed in the ADM-R with respect to the ADM-NR.

Contours of the average velocity at the lateral cross-section and downwind location $x/d = 5$ are shown in Fig. 7. The results show the non-axisymmetry (with respect to the turbine axis) of the velocity distribution due to the non-uniformity of the incoming flow and the presence of the surface. Simulation results of the mean resolved velocity obtained from both the ALM and the

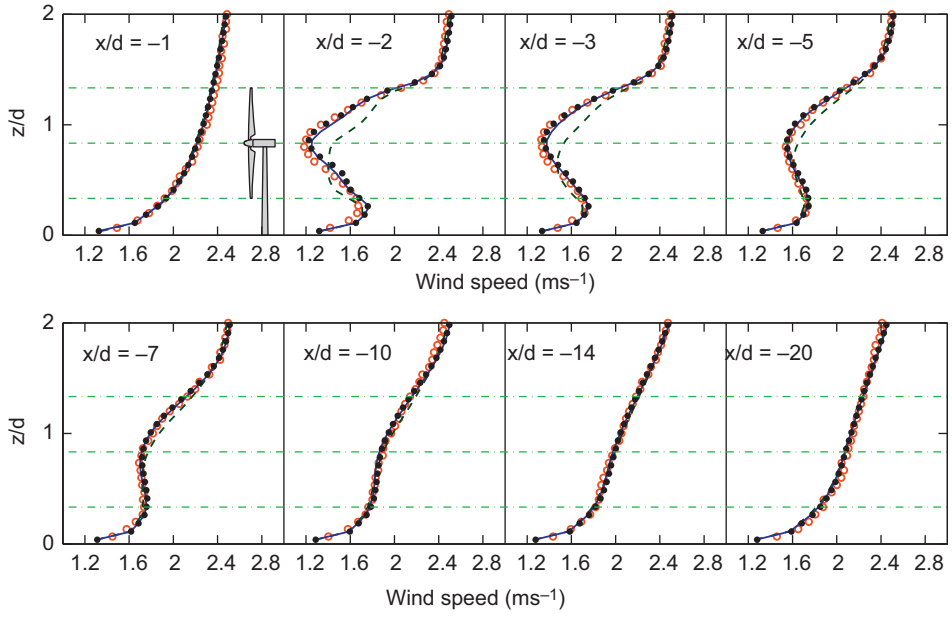

Fig. 6. Comparison of vertical profiles of the time-averaged streamwise velocity $\overline{u}$ (m/s): wind-tunnel measurements (◦), ADM-NR (dashed line), ADM-R (solid line) and ALM (dotted line).

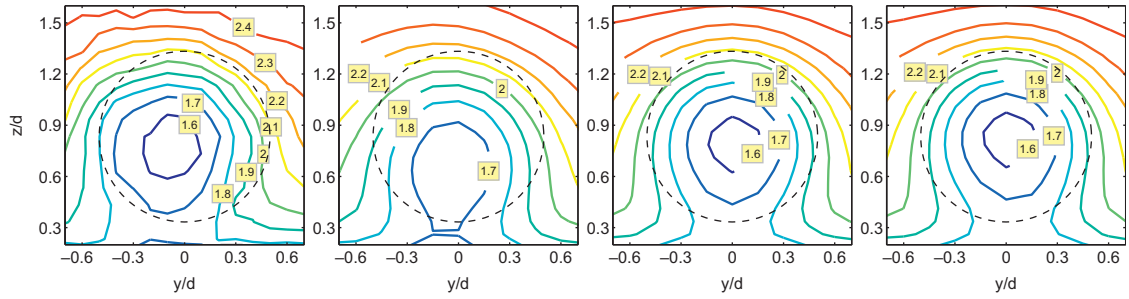

Fig. 7. Contours of the time-averaged streamwise velocity $\overline{u}$ (m/s) at the lateral cross-section and downstream $x/d=5$ obtained from the wind-tunnel measurements, ADM-NR, ADM-R and ALM (from left to right). The dashed line represents the turbine region.

ADM-R are in reasonable agreement with the measurements, with only a small difference in the magnitude of the velocity for both models. However, the ADM-NR yields a poor prediction of the mean velocity distribution in comparison with the wind-tunnel experimental data.

Fig. 8 shows contours of the streamwise turbulence intensity $\sigma_u/\overline{u}_{hub}$ obtained from the wind-tunnel measurements and simulations (resolved part) using LES with the ADM-NR, ADM-R and ALM on a vertical plane perpendicular to the turbine. Vertical profiles of measured and simulated turbulence intensities at

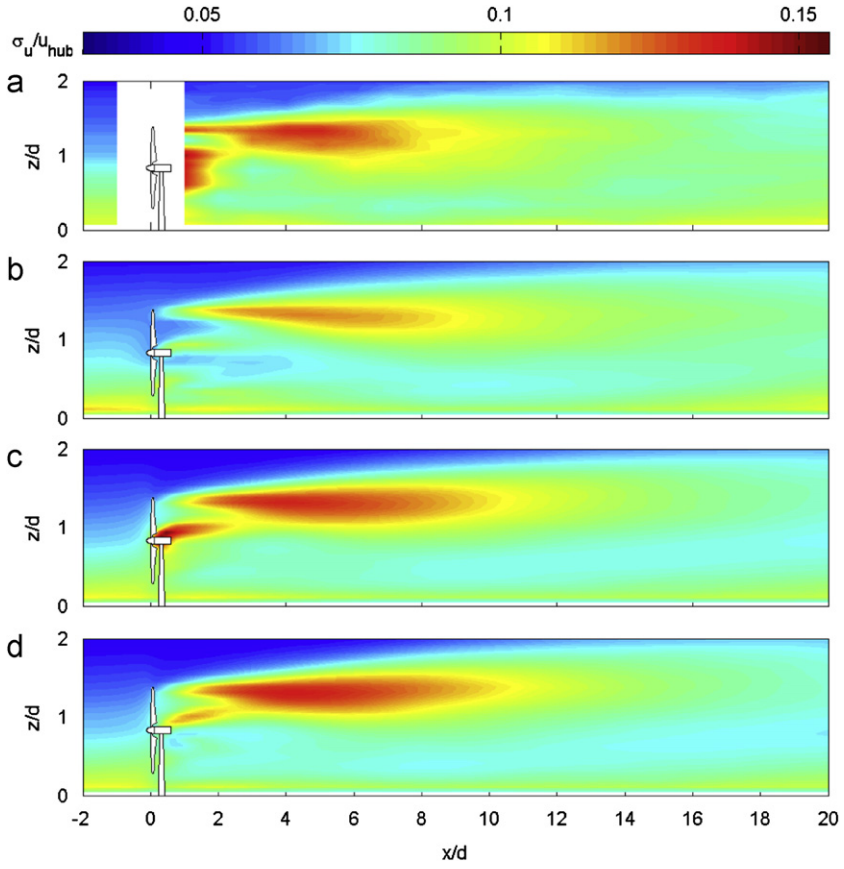

Fig. 8. Contours of the streamwise turbulence intensity $\sigma_u/\overline{u}_{hub}$ in the middle vertical plane perpendicular to the turbine: (a) wind-tunnel measurements, (b) ADM-NR, (c) ADM-R and (d) ALM.

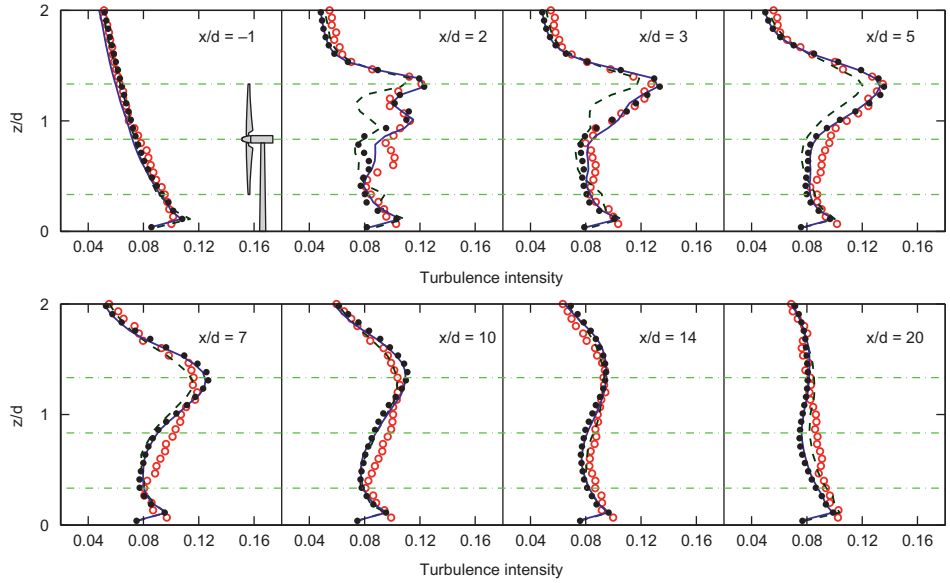

Fig. 9. Comparison of vertical profiles of the streamwise turbulence intensity $\sigma_u/\overline{u}_{hub}$: wind-tunnel measurements (◦), ADM-NR (dashed line), ADM-R (solid line) and ALM (dotted line).

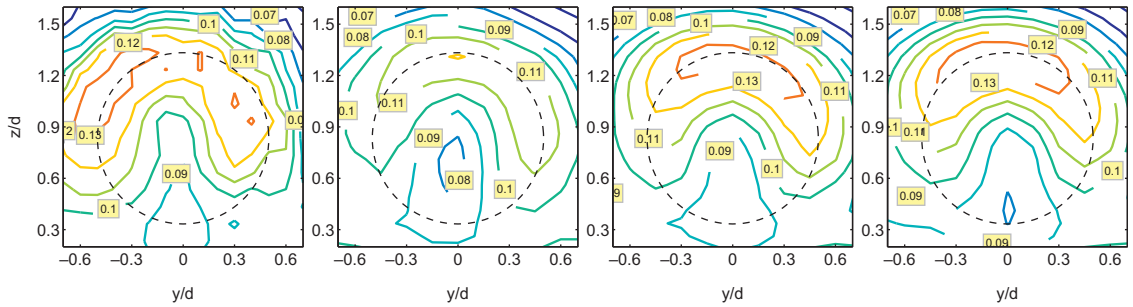

Fig. 10. Contours of the streamwise turbulence intensity $\sigma_u/\overline{u}_{hub}$ at the lateral cross-section and downstream $x/d=5$ obtained from the wind-tunnel measurements, ADM-NR, ADM-R and ALM (from left to right). The dashed line represents the turbine region.

selected downwind locations ($x/d=2$, 3, 5, 7, 10, 14, 20) are also shown in Fig. 9, together with the incoming flow turbulence intensity profile. As reported by Chamorro and Porté-Agel (2009, 2010), the measurements show a strong enhancement of the turbulence intensity (compared with the relatively low turbulence levels in the incoming flow) at the level of the top tip. The maximum turbulence intensity is found at that level and at a normalized distance of approximately $3<x/d<5$. It is important to point out that this is within a typical range of distances between adjacent wind turbines in wind farms and, therefore, it should be considered when calculating wind loads on the turbines. The turbulence intensity distribution and, in particular, the maximum enhancement of turbulence intensity occurring at the top-tip level can be explained considering the non-axisymmetric distribution of velocity profiles (Figs. 5 and 6) and the fact that the mean shear and associated turbulence kinetic energy production are maximum at the top-tip height. Simulations using the three wind-turbine models yield similar qualitative trends in the turbulence intensity distribution and the location of the maximum value. However, all models differ in their ability to capture the magnitude of the turbulence intensity. In particular, the turbulence intensity profiles obtained with both the ALM and the ADM-R are good agreement with the wind-tunnel measurements. The ADM-NR clearly underestimates the wake turbulence intensity at the downstream positions of $x/d=2$, 3 and 5, and therefore its maximum value. However, like in the case of the mean velocity, all wind-turbine models give a good prediction in the far-wake region, particularly after 10 rotor diameters.

Fig. 10 shows contour plots of the measured and simulated normalized turbulence intensity at the spanwise cross-section corresponding to the downwind distance $x/d=5$. Like in the case of the average velocity, the turbulence intensity from both measurements and simulations shows a clear non-axisymmetric distribution, with an inverse U-shape of the contour lines and a maximum turbulence intensity at the top-tip height. As explained above, this is the result of a non-uniform incoming flow and the presence of the surface. Consistent with the vertical profiles, for a given downwind distance, the maximum turbulence intensity is found at the top-tip height. Compared with the wind-tunnel experimental result, both the ALM and the ADM-R are much better able to predict the distribution and the magnitude of the turbulence intensity than the ADM-NR.

4. LES of flow through an operational wind farm

In this section, the above-described LES framework is applied to study the ABL flow through an operational wind farm. The wind farm chosen for this study occupies an area of approximately 11×11 km^2 of flat farm land located in Mower County, Minnesota. It is operated by NextEra Energy Resources, Inc. As shown in Fig. 11a, the wind farm consists of 43 Siemens SWT-2.3-93 turbines, which have a hub height of 80 m, a rotor diameter of 93 m, and a maximum power capacity of 2.3 MW. In this study, we focus on the simulation of ABL flow and its interactions with a subset of five wind turbines located in the southwest corner of the wind farm as shown in Fig. 11b. In particular, we study the structure of the wind-turbine wakes that form behind those five wind turbines. Supervisory Control And Data Acquisition (SCADA) data are available for each turbine in 10-min intervals.

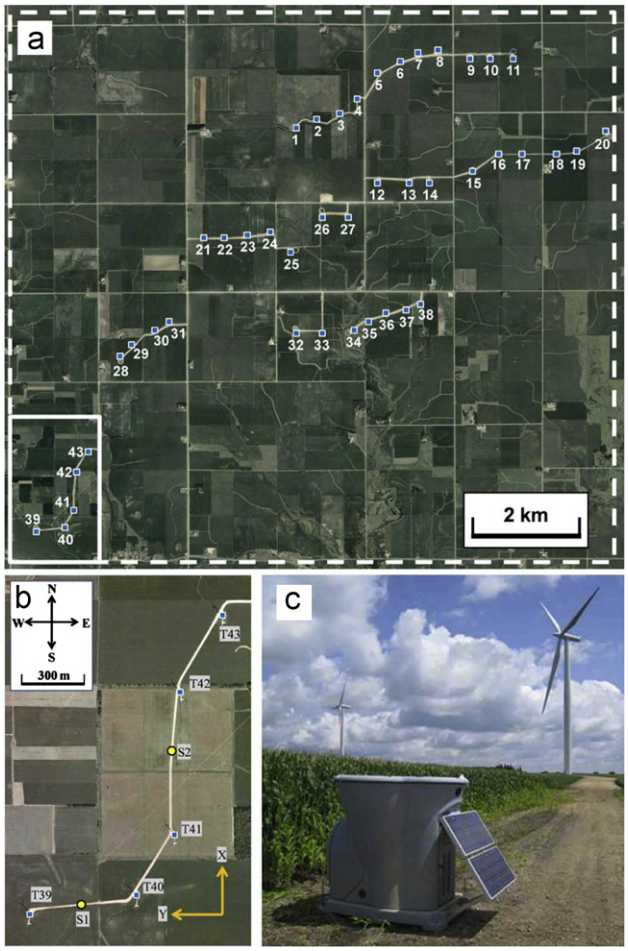

Fig. 11. (a) Map showing the layout of the Mower County wind farm. (b) Detailed map of the southwestern section of the farm, showing the location of the two SODARs (S1 and S2). (c) Picture of SODAR S1 and turbines T40 and T41.

Two SOnic Detection And Ranging (SODAR) instruments, provided by SecondWind, Inc., were deployed and used to measure vertical profiles of the mean wind velocity at two

locations in the wind farm (labeled S1 and S2 in Fig. 11b). The first SODAR (S1) was placed midway between turbines T39 and T40 with the intention of measuring the background atmospheric wind profile during periods when the wind was blowing from the south (the prevailing wind direction). Fig. 11c shows a picture of this SODAR and turbines T40 and T41. The second SODAR (S2) was placed between turbines T41 and T42 (specifically at a distance of four rotor diameters downwind of T41) with the intention of measuring the wake of T41 during southerly wind conditions. The SODARs measure the vertical wind profile using three beams, each 10° off the vertical, and separated horizontally by 120°. The half power beam width is approximately 11°. Pulses from each of these three beams are sent out at approximately 10 s intervals, and the return signals are averaged over a 10-min period to calculate the vertical wind profile. The measured wind profiles include all three components of velocity at heights of 40, 50, 60, 80, 100, 120, 140, 160, 180, and 200 m above ground level. Table 1 shows the coordinates of the two SODARs as well as the five wind turbines with respect to the *XY* reference system shown in Fig. 11b.

4.1. Case description

The period of November 22, 2009, between 2100 and 2200 UTC, was chosen for our case study because of the relatively simple and quasi-stationary atmospheric boundary layer conditions. During that period, atmospheric stability was near-neutral, atmospheric conditions were favorable for good SODAR echoes, and the wind blew from the south with quasi-stationary magnitude and direction. This study focuses on wind-turbine wakes in high-Reynolds-number neutrally stratified ABL flow, and therefore viscous, molecular, Coriolis and buoyancy effects are neglected in the simulations. Based on a semi-logarithmic fit of the velocity profile measured during the study period by the SODAR at the S1 location (not affected by turbine wakes), one can calculate a frictional velocity of $u_*=0.63$ m/s and a surface roughness of $z_0=0.3$ m. The size of the simulation domain is $L_x=2400$ m, $L_y=1200$ m and $L_z=700$ m in the streamwise, spanwise and vertical directions, respectively. The domain is divided uniformly into $N_x \times N_y \times N_z = 192 \times 192 \times 112$ grid points, with a spatial resolution of $\Delta_x = 12.5$ m and $\Delta_y = \Delta_z = 6.25$ m. As a result, each turbine rotor disk is covered by 15 points in both spanwise and vertical directions. A buffer zone technique is also implemented at a distance of four rotor diameters upwind of the wind farm to adjust the flow from the very-far-wake downwind condition to that of an undisturbed boundary layer inflow condition. The inflow condition is obtained from a separate simulation of the boundary-layer flow corresponding to the upwind of the wind farm in the field measurements.

Table 1
Positions of wind turbines and SODARs associated with the *XY* coordinate system shown in Fig. 11b.

	T39	T40	T41	T42	T43	S1	S2
X (m)	0	93	385	1062	1425	44	780
Y (m)	917	412	232	200	0	665	240

In the LESs of the wind farm case considered here, the wind-turbine-induced forces are modeled using the three models (ADM-NR, ADM-R and ALM) presented in Section 2. The SGS momentum flux is parameterized using the Lagrangian scale-dependent dynamic model. Some of the parameters required for the wind-turbine models, such as turbine angular velocity, turbine power output, and blade pitch angle, are obtained from the SCADA data set. During the one-hour period under consideration, the mean wind speed at the hub height was approximately 9 m/s, which leads to the Siemens SWT-2.3-93 turbines operating with a mean angular velocity of 15 rpm and producing a mean power of 1.4 MW. The geometry of the B45 blade that is part of the Siemens SWT-2.3-93 turbines is given by Leloudas (2006). Laursen et al. (2007) used computational fluid dynamics to characterize the angle of attack and the lift and drag coefficients along the B45 blade. In the ADM-NR, a constant and uniform thrust coefficient (C_T) is used in the simulation. To estimate this thrust coefficient based on the mean turbine power available from the SCADA data, we first compute the power coefficient (ratio of turbine power to power available in the wind) $C_p=0.47$. Then, assuming the mechanical efficiency of the turbine to be $\eta_{mech}=1$, and using the following relationships derived from one-dimensional momentum theory (Manwell et al., 2002),

$$C_p = 4a(1-a)^2 \tag{21}$$

and

$$C_T = 4a(1-a), \tag{22}$$

where a is the overall induction factor, we obtain $a=0.17$ and an overall thrust coefficient of $C_T=0.57$, which is then used in the ADM-NR. Due to the resolution limitations of LES, effects associated with the aeroelastic behavior of the turbines are not considered here. All simulations have been run for 1.5 h of real

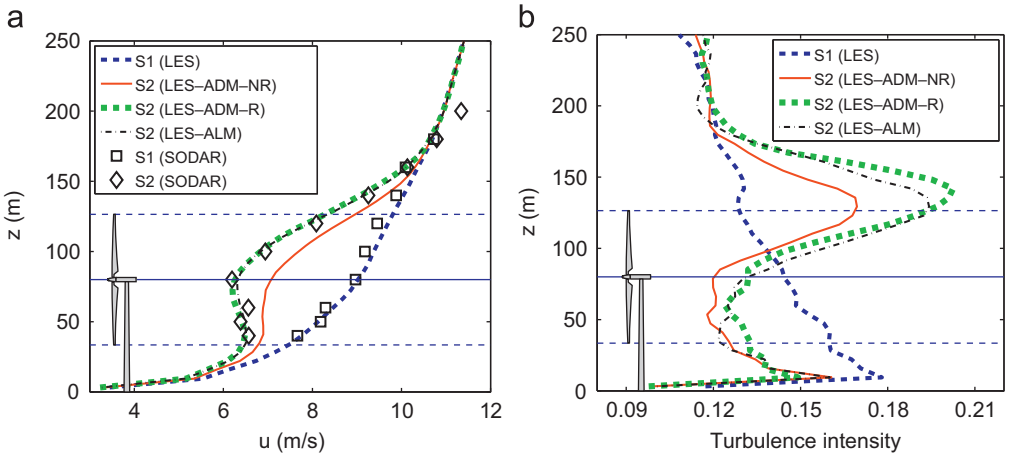

Fig. 12. Comparison of vertical profiles of time-averaged streamwise velocity $\overline{u}$ (m/s) (a) and streamwise turbulence intensity $\sigma_u/\overline{u}_{hub}$ (b) simulated at locations S1 and S2 using LES with different wind-turbine models. Also plotted are the mean wind velocity profiles measured with the two SODARs.

time to guarantee quasi-steady flow conditions. Results are presented here for the last half-hour of the simulations.

4.2. Simulation results

Fig. 12a shows the time-averaged streamwise velocity profiles at the S1 and S2 locations (see Fig. 11b) obtained from both SODAR measurements and numerical simulations. Overall, the velocity profiles obtained from the ADM-R and the ALM are in good agreement with the SODAR measurements. The ADM-NR slightly overestimates the magnitude of the velocity in the near-wake region. This slight underestimation of the velocity deficit by the ADM-NR is consistent with the simulation results on the wind-tunnel case (Section 3). As discussed in Section 3, this can be attributed to limitations of the two key assumptions made in the ADM-NR: ignoring turbine-induced rotation effects, and assuming uniform thrust distribution over the rotor disk.

Fig. 12b shows vertical profiles of the streamwise turbulence intensity obtained from simulations with the three wind-turbine models at the S1 and S2 locations. It is obvious that the three models yield an enhancement of the turbulence intensity at the top-tip level (compared with the relatively lower turbulence intensity in the incoming flow). This turbulence intensity enhancement has also been reported in wind-tunnel and LES studies, as described in Section 3. The magnitude of the maximum turbulence intensity obtained from both the ADM-R and the ALM is larger than the one from the ADM-NR, which is also consistent with the simulation results presented in Section 3 for the wind-tunnel case.

Two-dimensional contour plots of the simulated time-averaged streamwise velocity obtained with the three wind-turbine models on a horizontal plane at hub height, as well as on a vertical plane perpendicular to the middle of the rotor of turbine T41, are shown in Figs. 13 and 14, respectively. As expected, turbine wakes (regions of reduced mean velocity) are clearly visible behind each wind turbine. From Fig. 13, the effect of the wake induced by turbine T39 is still noticeable in the far-wake region at distances as far as 1700 m (approximately 18 rotor diameters downwind), which is consistent with the wind-tunnel observations. The largest velocity reduction, relative to the incoming boundary-layer flow, is observed in the wake of turbine T42. This is due to the fact that, for that wind direction, turbine T42 is located in the wake of turbine T41. Also consistent with the wind-tunnel case simulations presented in Section 3, the ADM-NR overestimates the magnitude of the near-wake velocity (thus underestimating the velocity deficit) compared with both ADM-R and ALM. In the case of the Siemens SWT-2.3-93 wind turbine, some differences are also observed between the near-wake mean velocity simulated with the ADM-R and ALM.

In order to understand the effect of the simulated wakes on turbine power reduction, the available wind power at one rotor diameter upwind of each turbine has been computed using $P = 0.5\rho A\overline{U}^3_{rotor}$, where $\overline{U}_{rotor}$ is the average velocity integrated over the whole rotor area (A). It should be noted that the wake induced by turbine T41 results in a substantial power reduction ($r_P \equiv (1-P_{T42}/P_{T41}) \times 100\%$) on the flow upwind of turbine T42. The r_p values obtained from the simulations with ALM and ADM-R are, respectively, 47% and 50%, which are very close to the actual wind turbine power reduction of 48% based on the SCADA data. The ADM-NR yields a lower power reduction value of 37%, due to the overprediction of the velocity magnitude in the wake induced by turbine T41.

Two-dimensional contour plots of the time-averaged vertical velocity component, simulated using LES with the three wind-turbine models, are shown in Fig. 15 for a horizontal plane at hub height. The positive and negative vertical velocities obtained with the ADM-R and ALM on both sides of the wakes highlight the ability of those models to induce wake rotation. As expected, the wakes rotate in counter-clockwise direction (for an observer located upwind of the turbine), which is opposite to the clockwise rotation of the turbine blades. It should be noted that the vertical

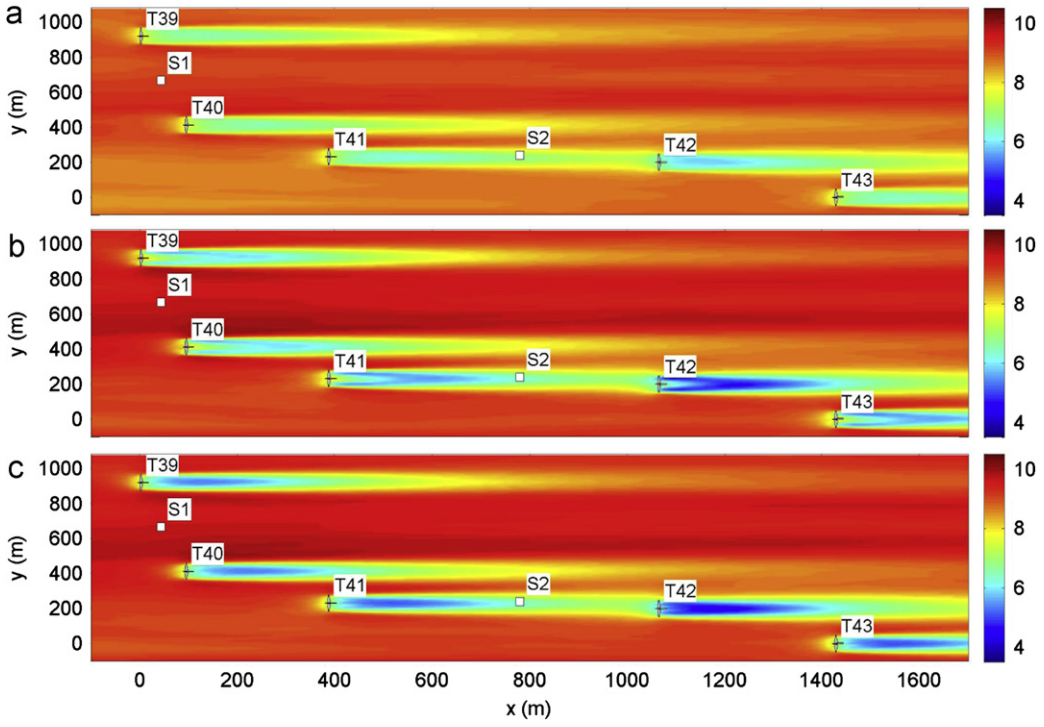

Fig. 13. Two-dimensional contour plots of the simulated time-averaged streamwise velocity $\overline{u}$ (m/s) on a horizontal plane at hub height: (a) ADM-NR, (b) ADM-R and (c) ALM.

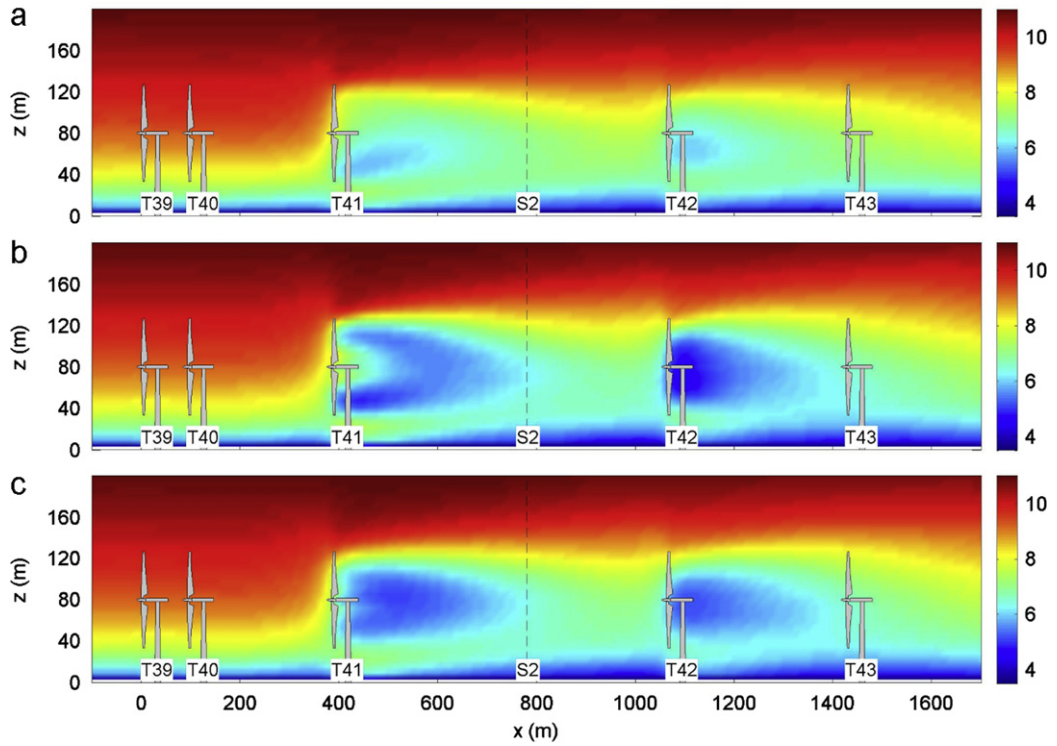

Fig. 14. Two-dimensional contour plots of the simulated time-averaged streamwise velocity $\overline{u}$ (m/s) on a vertical plane perpendicular to the rotor (and through the middle) of turbine T41: (a) ADM-NR, (b) ADM-R and (c) ALM.

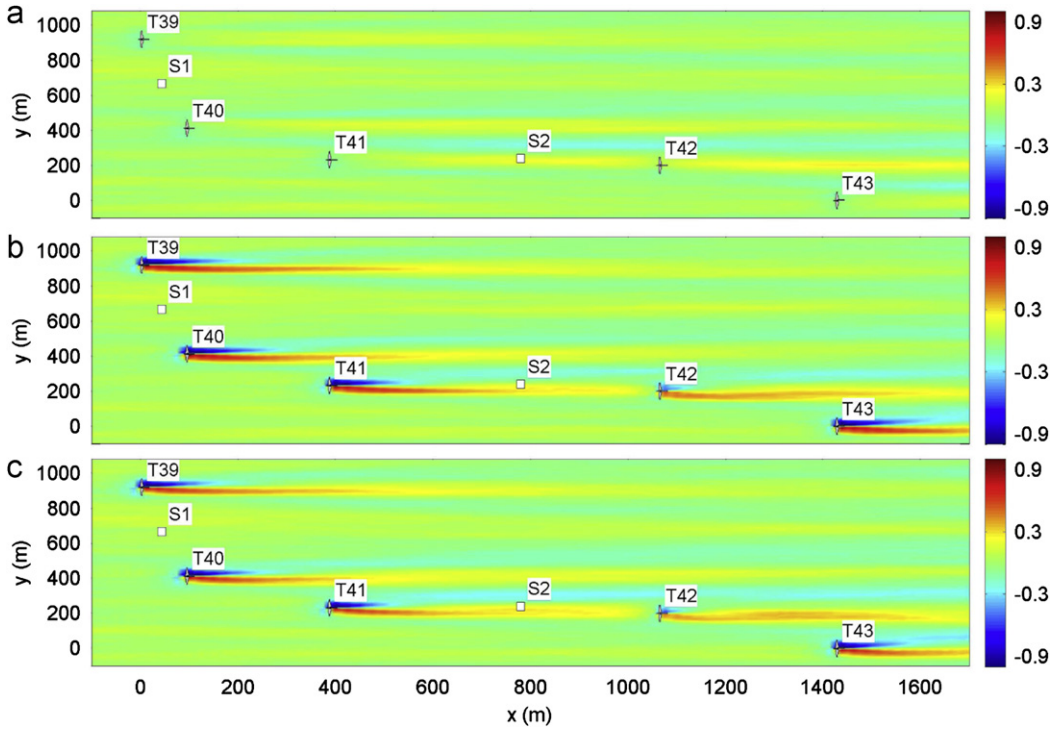

Fig. 15. Two-dimensional contour plots of the simulated time-averaged vertical velocity $\overline{w}$ (m/s) on a horizontal plane at hub height: (a) ADM-NR, (b) ADM-R and (c) ALM.

velocity distribution in the wakes is non-symmetric, with the positive velocity region extending further downwind compared with the negative velocity. The non-axisymmetry of the wake is consequence of the interactions of the rotating wake flow with both the land surface and the non-uniform (logarithmic) incoming boundary layer flow. Note that the ADM-NR is unable to account for wake rotation because it only considers the thrust force and ignores any forces parallel to the rotor plane, which are responsible for the rotation of the wake flow.

Two-dimensional contours of the simulated streamwise turbulence intensity obtained with the three wind-turbine models on a vertical plane perpendicular to the middle of the rotor of turbine T41 are shown in Fig. 16. From that figure, it is clear that the three turbine models lead to an enhancement of the

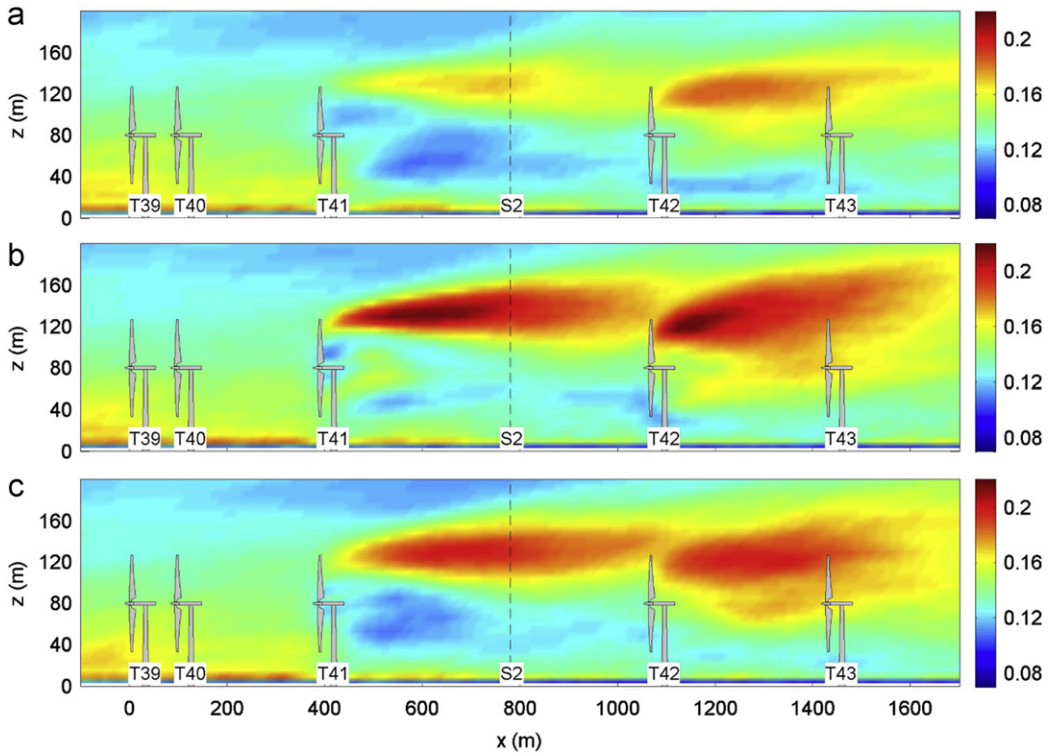

Fig. 16. Two-dimensional contour plots of the simulated streamwise turbulence intensity $\sigma_u/\overline{u}_{hub}$ on a vertical plane perpendicular to the rotor (and through the middle) of turbine T41: (a) ADM-NR, (b) ADM-R and (c) ALM.

turbulence intensity at the top-tip height. The maximum simulated turbulence intensity at that height is higher (by about 20%) than the one observed for the wind-tunnel case. However, owing to the larger turbulence levels in the incoming flow for the field case, the increase in the turbulence intensity (with respect to the incoming flow levels) is similar for both cases. Furthermore, the maximum turbulence intensity at that height is found at a normalized distance of approximately $1 < x/d < 3$ downwind of turbines T41 and T42. It should be noted that this distance from the wind turbines to the peak of turbulence intensity is shorter than the one found for the wind-tunnel case (approximately $3 < x/d < 5$, as shown in Fig. 8). This result is consistent with previous observations that the extent of the near-wake region measured in wind-tunnel experiments is typically longer than that measured in the field (Helmis et al., 1995). It also highlights some of the challenges associated with the design of wind-tunnel experiments to study the structure and dynamics of wind-turbine wakes, especially in the near-wake region, where the details of the blades and the incoming flow characteristics (e.g., turbulence intensity) are likely to play an important role.

5. Summary

This paper presents recent efforts to develop and validate a large-eddy simulation framework for wind energy applications. The tuning-free Lagrangian scale-dependent dynamic models are used to parameterize the SGS stress tensor and the SGS heat flux. Three types of models are used to parameterize the turbine-induced forces: a standard actuator-disk model without rotation (ADM-NR) that computes an overall thrust force and distributes it uniformly over the rotor disk area; an actuator-disk model with rotation (ADM-R) that computes the local lift and drag forces (based on blade-element momentum theory) and distributes them on the rotor disk area; and an actuator-line model (ALM) that distributes those forces along lines that follow the position of the blades.

The proposed LES framework is validated against high-resolution velocity measurements collected in the wake of a miniature wind turbine placed in a wind-tunnel boundary layer flow. In general, the characteristics of the simulated turbine wakes (average velocity and turbulence intensity distributions) are in good agreement with the measurements. The comparison with the wind-tunnel measurements shows that the turbulence statistics obtained with the LES and the ADM-NR have some differences with respect to the measurements in the near-wake region. In particular, the model overestimates the average velocity in the center of the wake, while underestimating the turbulence intensity at the top-tip level, where turbulence levels are highest due to the presence of a strong shear layer. The ADM-R and ALM yield more accurate predictions of the different turbulence statistics in the near-wake region. This highlights the importance of using a wind-turbine model that induces wake rotation and allows for non-uniform distribution of the turbine-induced forces. In the far wake, all three models produce reasonable results.

The proposed LES framework is also used to simulate ABL flow through an operational wind farm, where SODAR measurements are available at two locations. Again, the ADM-R and the ALM are capable of delivering accurate mean velocity profiles in the wake, with ADM-NR slightly underestimating the velocity deficit in the near wake. The characteristics (velocity deficit and turbulence intensity) of the simulated wakes behind the field-scale Siemens SWT-2.3-93 turbines show similar qualitative behavior compared with the stand-alone turbine wake measured in the wind tunnel. However, some quantitative differences have been found; the peak of the turbulence intensity is larger (by about 20%) and it appears at a relatively shorter downwind distance from the turbine, compared with the wind-tunnel case. These differences

are consistent with observations from previous wind-tunnel and field studies of wind-turbine wakes (Vermeer et al., 2003), and they can be attributed to differences in the turbines and the incoming flow characteristics (e.g., turbulence intensity) between the wind tunnel and the field. Regarding turbine power prediction, simulations with both ADM-R and ALM are able to predict reductions in power associated with turbine wakes. Consistent with the underestimation of the velocity deficit, the ADM-NR is found to underestimate the power reduction in turbines operating in wakes of other turbines.

The research presented here constitutes a step towards the development and the validation of a robust computational fluid dynamics framework for the study of atmospheric boundary layer flow and its interactions with wind turbines and wind farms. This framework can be used to optimize the design (turbine siting) of wind energy projects (single turbines and wind farms) by increasing the efficiency, energy output and lifetime of wind turbines. It can also be used to study the effects of wind farms on local meteorology. Future efforts will focus on further development, validation and application of this LES framework in a variety of cases involving different atmospheric stability conditions (neutral, stable and unstable), land-surface characteristics (land cover and topography) and wind-farm layouts.

Acknowledgments

This research was supported by the Swiss National Science Foundation (Grant 200021_132122), the National Science Foundation (Grants EAR-0537856 and ATM-0854766), NASA (Grant NNG06GE256), customers of Xcel Energy through a Grant (RD3-42) from the Renewable Development Fund, and the University of Minnesota Institute for Renewable Energy and the Environment. Computing resources were provided by the Minnesota Supercomputing Institute. The SODARs were provided by SecondWind, Inc., and Barr Engineering Company assisted with their deployment.

References

AGARD, 1998. A selection of test cases for the validation of large-eddy simulations of turbulent flows. AGARD Advisory Report 345.

Albertson, J.D., Parlange, M.B., 1999. Surface length scales and shear stress: implications for land–atmosphere interaction over complex terrain. Water Resour. Res. 35, 2121–2132.

Alinot, C., Masson, C., 2002. Aerodynamic simulations of wind turbines operating in atmospheric boundary layer with various thermal stratifications. In: ASME Wind Energy Symposium AIAA, 2002-42.

Arya, S.P., 2001. Introduction to Micrometeorology, second ed. vol. 79. Academic Press.

Baidya Roy, S., Pacala, S.W., Walko, R.L., 2004. Can large wind farms affect local meteorology? J. Geophys. Res. 109, 1–6.

Bou-Zeid, E., Vercauteren, N., Meneveau, C., Parlange, M., 2008. Scale dependence of subgrid-scale model coefficients: an a priori study. Phys. Fluids 20, 115106.

Businger, J.A., Wynagaard, J.C., Izumi, Y., Bradley, E.F., 1971. Flux–profile relationships in the atmospheric surface layer. J. Atmos. Sci. 28, 181–189.

Calaf, M., Meneveau, C., Meyers, J., 2010. Large eddy simulation study of fully developed wind-turbine array boundary layers. Phys. Fluids 22, 015110.

Chamorro, L.P., Porté-Agel, F., 2009. A wind-tunnel investigation of wind-turbine wakes: boundary-layer turbulence effects. Boundary-Layer Meteorol. 132, 129–149.

Chamorro, L.P., Porté-Agel, F., 2010. Effects of thermal stability and incoming boundary-layer flow characteristics on wind-turbine wakes: a wind-tunnel study. Boundary-Layer Meteorol., 515–533.

Crespo, A., Hernández, J., 1996. Turbulence characteristics in wind-turbine wakes. J. Wind Eng. Ind. Aerodyn. 61, 71–85.

Froude, R.E., 1889. On the part played in propulsion by difference of fluid pressure. Trans. R. Inst. Naval Arch. 30, 390–423.

Germano, M., Piomelli, U., Cabot, W.H., 1991. A dynamic subgrid-scale eddy viscosity model. Phys. Fluids A 3, 1760–1765.

Glauert, H., 1963. Airplane propellers. In: Durand, W.F. (Ed.), Aerodynamic Theory. Dover, New York, pp. 169–360.

Gómez-Elvira, R., Crespo, A., Migoya, E., Manuel, F., Hernández, J., 2005. Anisotropy of turbulence in wind turbine wakes. J. Wind. Eng. Ind. Aerodyn. 93, 797–814.

Gong, W., Taylor, P.A., Därnbrack, A., 1996. Turbulent boundary-layer flow over fixed aerodynamically rough two-dimensional sinusoidal waves. J. Fluid Mech. 312, 1–37.

Helmis, C.G., Papadopoulos, K.H., Asimakopoulos, D.N., Papageorgas, P.G., Soilemes, A.T., 1995. An experimental study of the near wake structure of a wind turbine operating over complex terrain. Sol. Energy 54, 413–428.

Ivanell, S., Sørensen, J.N., Mikkelsen, R., Henningson, D., 2009. Analysis of numerically generated wake structures. Wind Energy 12, 63–80.

Jimenez, A., Crespo, A., Migoya, E., Garcia, J., 2007. Advances in large-eddy simulation of a wind turbine wake. J. Phys. Conf. Ser. 75, 012041.

Jimenez, A., Crespo, A., Migoya, E., Garcia, J., 2008. Large-eddy simulation of spectral coherence in a wind turbine wake. Environ. Res. Lett. 3, 015004.

Kasmi, A.E., Masson, C., 2008. An extended $\kappa-\varepsilon$ model for turbulent flow through horizontal-axis wind turbines. J. Wind. Eng. Ind. Aerodyn. 96, 103–122.

Kleissl, J., Meneveau, C., Parlange, M.B., 2003. On the magnitude and variability of subgrid-scale eddy-diffusion coefficients in the atmospheric surface layer. J. Atmos. Sci. 60, 2372–2388.

Kleissl, J., Parlange, M.B., Meneveau, C., 2004. Field experimental study of dynamic Smagorinsky models in the atmospheric surface layer. J. Atmos. Sci. 61, 2296–2307.

Laursen, J., Enevoldsen, P., Hjort, S., 2007. 3D CFD rotor computations of a multi megawatt HAWT rotor. In: European Wind Energy Conference, Milan, Italy.

Leloudas, G., 2006. Optimization of wind turbines with respect to noise. Masters Thesis Project, MEK, DTU.

Lilly, D.K., 1967. The representation of small-scale turbulence in numerical simulation experiments. In: Proceedings of IBM Scientific Computing Symposium on Environmental Sciences. IBM Data Processing Division, White Plains, NY, p. 195.

Lilly, D.K., 1992. A proposed modification of the Germano subgrid-scale closure method. Phys. Fluids 4, 633–635.

Manwell, J., McGowan, J., Rogers, A., 2002. Wind Energy Explained: Theory, Design and Application. Wiley, New York.

Mason, P.J., 1994. Large-eddy simulation: a critical review of the technique. Q. J. R. Meteorol. Soc. 120, 1–26.

Mason, P.J., Brown, A.R., 1999. On subgrid models and filter operations in large eddy simulations. J. Atmos. Sci. 56, 2101–2114.

Mason, P.J., Derbyshire, S.H., 1990. Large-eddy simulation of the stably-stratified atmospheric boundary layer. Boundary-Layer Meteorol. 53, 117–162.

Mason, P.J., Thomson, D.J., 1992. Stochastic backscatter in large-eddy simulations of boundary layers. J. Fluid Mech. 242, 51–78.

Medici, D., Alfredsson, P.H., 2006. Measurements on a wind turbine wake: 3D effects and bluff body vortex shedding. Wind Energy 9, 219–236.

Meneveau, C., Lund, T.S., Cabot, W.H., 1996. A lagrangian dynamic subgrid-scale model of turbulence. J. Fluid Mech. 319, 353–385.

Moeng, C.H., 1984. A large-eddy-simulation model for the study of planetary boundary-layer turbulence. J. Atmos. Sci. 41, 2052–2062.

Moin, P., Squires, K.D., Lee, S., 1991. A dynamic subgrid-scale model for compressible turbulence and scalar transport. Phys. Fluids 3, 2746–2757.

Petersen, E.L., Mortensen, N.G., Landberg, L., Højstrup, J., Frank, H.P., 1998. Wind power meteorology. Part 1: climate and turbulence. Wind Energy 1, 25–45.

Pope, S.B., 2000. Turbulent Flows. Cambridge University Press, Cambridge.

Porté-Agel, F., 2004. A scale-dependent dynamic model for scalar transport in large-eddy simulations of the atmospheric boundary layer. Boundary-Layer Meteorol. 112, 81–105.

Porté-Agel, F., Meneveau, C., Parlange, M.B., 2000. A scale-dependent dynamic model for large-eddy simulation: application to a neutral atmospheric boundary layer. J. Fluid Mech. 415, 261–284.

Porté-Agel, F., Meneveau, C., Parlange, M.B., Eichinger, W.E., 2001. A priori field study of the subgrid-scale heat fluxes and dissipation in the atmospheric surface layer. J. Atmos. Sci. 58, 2673–2698.

Rankine, W.J.M., 1865. On the mechanical principles of the action of propellers. Trans. R. Inst. Naval Arch. 6, 13–39.

Sagaut, P., 2006. Large Eddy Simulation for Incompressible Flows, third ed. Springer-Verlag, Berlin, Heidelberg.

Sezer-Uzol, N., Long, L.N., 2006. 3-D time-accurate CFD simulations of wind turbine rotor flow fields. AIAA Paper 2006-0394.

Smagorinsky, J., 1963. General circulation experiments with the primitive equations: I. The basic experiment. Mon. Weather Rev. 91, 99–164.

Sørensen, J.N., Shen, W.Z., 2002. Numerical modeling of wind turbine wakes. J. Fluids Eng. 124, 393–399.

Sørensen, N.N., Michelsen, J.A., Schreck, S., 2002. Navier-stokes predictions of the NREL phase VI rotor in the NASA Ames 80 ft $\times$ 120 ft wind tunnel. Wind Energy 5, 151–169.

Stoll, R., Porté-Agel, F., 2006a. Dynamic subgrid-scale models for momentum and scalar fluxes in large-eddy simulations of neutrally stratified atmospheric boundary layers over heterogeneous terrain. Water Resour. Res. 42, W01409.

Stoll, R., Porté-Agel, F., 2006b. Effect of roughness on surface boundary conditions for large-eddy simulation. Boundary-Layer Meteorol. 118, 169–187.

Stoll, R., Porté-Agel, F., 2008. Large-eddy simulation of the stable atmospheric boundary layer using dynamic models with different averaging schemes. Boundary-Layer Meteorol. 126, 1–28.

Sunada, S., Sakaguchi, A., Kawachi, K., 1997. Airfoil section characteristics at a low Reynolds number. J. Fluids Eng. 119, 129–135.

Tongchitpakdee, C., Benjanirat, S., Sankar, L.N., 2005. Numerical simulation of the aerodynamics of horizontal axis wind turbines under yawed flow conditions. J. Sol. Energy Eng. 127, 464–474.

Troldborg, N., Sørensen, J.N., Mikkelsen, R., 2007. Actuator line simulation of wake of wind turbine operating in turbulent inflow. J. Phys. Conf. Ser. 75, 012063.

Vermeer, L.J., Sørensen, J.N., Crespo, A., 2003. Wind turbine wake aerodynamics. Prog. Aerosp. Sci. 39, 467–510.

Wan, F., Porté-Agel, F., 2011. Large-eddy simulation of stably-stratified flow over a steep hill. Boundary-Layer Meteorol., doi: 10.1007/s10546-010-9562-4.

Wan, F., Porté-Agel, F., Stoll, R., 2007. Evaluation of dynamic subgrid-scale models in large-eddy simulations of neutral turbulent flow over a two-dimensional sinusoidal hill. Atmos. Environ. 41, 2719–2728.

Wu, Y.T., Porté-Agel, F., 2011. Large-eddy simulation of wind-turbine wakes: evaluation of turbine parametrisations. Boundary-Layer Meteorol., doi: 10.1007/s10546-010-9569-x.

Xu, G., Sankar, L.N., 2000. Computational study of horizontal axis wind turbines. J. Sol. Energy Eng. 122, 35–39.